Insensitivity of a turbulent laser-plasma dynamo to initial conditions

A.F.A. Bott, ^{1,2} L. Chen, ¹ P. Tzeferacos, ^{1,3,4} C.A.J. Palmer, ⁵ A.R. Bell, ⁶ R. Bingham, ^{7,8} A. Birkel, ⁹ D.H. Froula, ^{3,4} J. Katz, ⁴ M.W. Kunz, ² C.-K. Li, ⁹ H-S. Park, ¹⁰ R. Petrasso, ⁹ J.S. Ross, ¹⁰ B. Reville, ¹¹ D. Ryu, ¹² F.H. Séguin, ⁹ T.G. White, ¹³ A.A. Schekochihin, ¹ D.Q. Lamb, ¹⁴ and G. Gregori^{1,14}

1) Department of Physics, University of Oxford, Oxford, UK

²⁾Department of Astrophysical Sciences, University of Princeton, Princeton, USA

³⁾Department of Physics and Astronomy, University of Rochester, Rochester, USA

⁴⁾Laboratory for Laser Energetics, University of Rochester, Rochester, USA

⁵⁾School of Mathematics and Physics, Queens University Belfast, Belfast, UK

⁶⁾Department of Physics, University of Oxford, Oxford, UK

7) Rutherford Appleton Laboratory, Chilton, Didcot, UK

8) Department of Physics, University of Strathclyde, Glasgow, UK

⁹⁾Massachusetts Institute of Technology, Cambridge, USA

¹⁰⁾Lawrence Livermore National Laboratory, Livermore, USA

¹¹⁾Max-Planck-Institut für Kernphysik, Heidelberg, Germany

¹²⁾Department of Physics, School of Natural Sciences, UNIST, Ulsan, Korea

¹³⁾Department of Physics, University of Nevada, Reno, Nevada 89557, USA

¹⁴⁾Department of Astronomy and Astrophysics, University of Chicago, Chicago, USA

(*Electronic mail: abott@princeton.edu)

(Dated: 20 May 2022)

It has recently been demonstrated experimentally that a turbulent plasma created by the collision of two inhomogeneous, asymmetric, weakly magnetised laser-produced plasma jets can generate strong stochastic magnetic fields via the small-scale turbulent dynamo mechanism, provided the magnetic Reynolds number of the plasma is sufficiently large. In this paper, we compare such a plasma with one arising from two pre-magnetised plasma jets whose creation is identical save for the addition of a strong external magnetic field imposed by a pulsed magnetic field generator ('MIFEDS'). We investigate the differences between the two turbulent systems using a Thomson-scattering diagnostic, X-ray self-emission imaging and proton radiography. The Thomson-scattering spectra and X-ray images suggest that the presence of the external magnetic field has a limited effect on the plasma dynamics in the experiment. While the presence of the external magnetic field induces collimation of the flows in the colliding plasma jets and the initial strengths of the magnetic fields arising from the interaction between the colliding jets are significantly larger as a result of the external field, the energy and morphology of the stochastic magnetic fields post-amplification are indistinguishable. We conclude that, for turbulent laser-plasmas with super-critical magnetic Reynolds numbers, the dynamo-amplified magnetic fields are determined by the turbulent dynamics rather than the seed fields and modest changes in the initial flow dynamics of the plasma, a finding consistent with theoretical expectations and simulations of turbulent dynamos.

I. INTRODUCTION

The origin of the dynamically significant magnetic fields in the ionized gases that inhabit the space between clustered galaxies — the so-called intracluster medium (ICM) – is a problem that has occupied astrophysicists for over half a century^{1,2}. One of the most plausible mechanisms that can account for the strength of such magnetic fields is the smallscale turbulent dynamo, whereby turbulent bulk motions of a conducting fluid or plasma cause the efficient amplification of magnetic fields until they possess energies that are a non-negligible fraction of the kinetic energy of the driving turbulent motions^{3,4}. A significant number of analytical calculations⁵⁻⁸ and simulations within the framework of resistive magnetohydrodynamics (MHD)^{9–19} support the efficacy of this mechanism provided the magnetic Reynolds number Rm of the plasma (defined as Rm $\equiv u_{\rm rms}L/\eta$, where $u_{\rm rms}$ is the root-mean-square (rms) magnitude of the turbulent motions, L is the characteristic scale of those motions, and η the plasma's resistivity) exceeds some critical value $Rm_c \approx 50$ -

Of particular importance is the expectation that the charac-

teristic strength of the magnetic field post-amplification primarily depends on the turbulent kinetic energy provided Rm is supercritical (viz., $Rm > Rm_c$)^{15,19}. This expectation arises because the induction equation that is thought to describe the magnetic field's evolution is linear in the magnetic field, and so the saturation of dynamo-amplified fields must involve the back-reaction of the Lorentz force on the turbulent flow dynamics. Previous studies have shown that this back-reaction facilitates saturation via a combination of weakened stretching of magnetic field lines and relative enhancement of magnetic diffusion compared to stretching^{13,21,22}. This saturation mechanism sets the precise strengths at which magnetic fields are maintained, a quantity of great significance in astrophysical contexts^{23–25}. It also allows amplification of the initial magnetic energy over many orders of magnitude if it is much smaller than the turbulent kinetic energy. In many astrophysical environments, this property is crucial for resolving the vast discrepancy between the characteristic magnitudes of the observed dynamical fields, and seed magnetic fields generated by processes that can produce magnetic fields in unmagnetized plasmas (such as the Biermann battery^{1,26}).

By contrast, prior research suggests that the dynamo-

amplified magnetic fields are insensitive to both the strength of initial seed magnetic fields and specific particularities of the turbulent motions before amplification. For example, analytic studies of the 'Kazantsev' dynamo (which has a deltacorrelated in time velocity field) have shown that, during the kinematic phase of this model, any smooth initial spectrum of seed magnetic fields tends towards a characteristic Kazantsev spectrum that does not depend on the initial conditions^{5,8}. This result also holds in some generalised analytic models with finite correlation times²⁷. In addition, a recent numerical study²⁸ found that, for a Rm-supercritical turbulent flow in a periodic box, information about the strength and statistics of the initial seed magnetic fields was not retained in the saturated state of the associated small-scale turbulent dynamo.

In the last two decades, it has become possible to explore dynamo processes in controlled laboratory experiments. Historically, the first such experiments involved liquid-metal flows, which yielded many significant results: the first kinematic dynamo flow²⁹, dynamo saturation³⁰, and dynamo action in a partially stochastic flow³¹. However, liquid-metal experiments are limited to certain parameter regimes: incompressible flows whose magnetic Prandtl number Pm (defined as Pm $\equiv v/\eta$, where v is the fluid viscosity) is much smaller than unity. Since Pm is known to be an important parameter for the operation of turbulent dynamos¹⁵, and is large in many astrophysical environments¹³, alternative experimental approaches are needed. A series of recent laser-plasma experiments in which turbulent plasmas are created using grids have started to satisfy this need, producing a series of notable results: first the demonstration of the amplification of seed magnetic fields generated by the Biermann battery^{32–35}, and then the operation of a *bona fide* small-scale turbulent dynamo in a plasma with $Rm \approx 600^{36,37}$. In the last year, another laserplasma experiment provided time-resolved measurements of the action of a small-scale turbulent dynamo with $Rm \approx 450$, and also accessed the Pm ~ 1 regime for the first time in the laboratory³⁸. This advance was possible thanks to design improvements to the platform³⁹: specifically, changes in the material composition of the plasma and a new, optimised grid design. Amplification of magnetic fields (but not yet dynamo) was also observed in a supersonic turbulent laser-plasma⁴⁰, an experiment that was based on the first successful realisation of boundary-free supersonic turbulence in the laboratory⁴¹. Most recently, a turbulent laser-plasma with Rm $\approx 3,500$, $Pm \approx 10$, was successfully produced on the National Ignition Facility, with dynamo-amplified magnetic fields of megagauss strengths being observed⁴².

One finding of previous turbulent-dynamo experiments that merited further study was the ratio of the magnetic to turbulent kinetic energy-density, which was observed to be finite, but still quite small $(\epsilon_B/\epsilon_{K,turb}\approx 3\text{-}4\%)^{37,38}$. This prompted the question of whether the characteristic post-amplification strength of magnetic fields in these turbulent laser-plasmas is determined by the plasma's turbulent kinetic energy alone, or was in fact not dynamical and thus might be expected to be increased by a stronger initial magnetic field. In this paper, we discuss results from a new experiment (in the Pm ~ 1 regime) on the Omega Laser Facility 43 that demonstrates the former

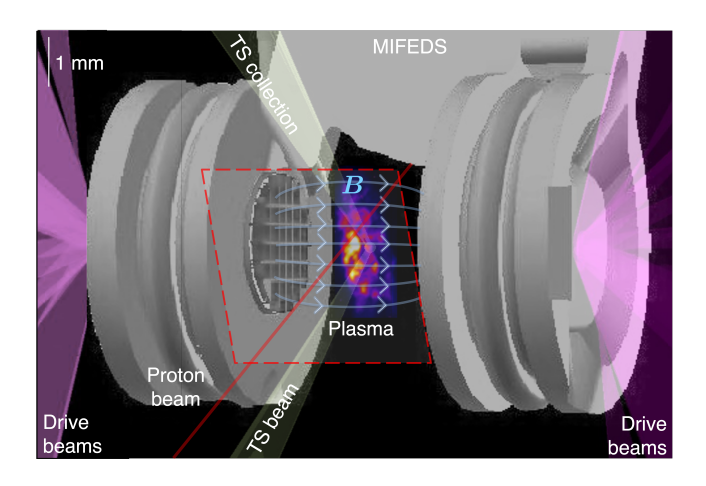


FIG. 1. Experimental set-up. Schematic of the experimental platform. Twenty beams of the OMEGA laser deliver a total of 10 kJ of 351-nm wavelength laser-light energy over 10 ns to an 800-µm diameter focal spot on two CH plastic foils (5 kJ/foil). The foils have the same design used on a previous experiment on the Omega Laser Facility³⁸: the primary foils have thicknesses of 50 μ m and are attached to annular washers with outer diameter of 3 mm, central-hole diameter of 400 μ m, and a thickness of 230 μ m. The grids used on the target are also the same; they have 300 μ m square holes and 100 μ m wires (periodicity $L \approx 400 \mu$ m), and are asymmetric, with the midpoints of the holes in one grid always facing the midpoints of the wire intersections in the other. The MIFEDS is operated at 19 kV, with maximum voltage coinciding with drive-beam initiation; the morphology of the initial magnetic field is indicated in light blue. The location of the interaction-region plasma is indicated, as is the Thomson scattering probe beam's path (in yellow). The central axis of the proton-radiography beam and the area probed by it are indicated in red.

claim. This demonstration is made by introducing a seed magnetic field into a turbulent laser-plasma with $Rm > Rm_{\rm c}$ whose energy is over an order of magnitude larger than the energy of the seed field arising inherently in the plasma. The stochastic magnetic fields that arise from the action of the small-scale turbulent dynamo on the seed field are then compared with a control case (viz., a plasma without an enhanced seed field). The key result is that the characteristic strengths and structure of the magnetic fields are indistinguishable with or without the enhanced seed field and its modest effect on the initial flow dynamics of the plasma.

II. EXPERIMENTAL DESIGN

The schematic of the experimental platform is shown in Figure 1, with detailed target specifications given in the caption. The target platform design is related to previous experiments on the Omega Laser Facility ^{37,38,44}: a turbulent plasma is created by colliding rear-side blow-off plasma jets that, prior to their collision, have passed through asymmetric grids. On collision, an 'interaction region' of plasma forms which has higher characteristic densities and ion/electron temperatures than either jet. In addition, the asymmetric heterogeneity

of the jets leads to the formation of strong shear flows in the interaction-region plasma. These become Kelvin-Helmholtz unstable and turbulent motions quickly develop.

The experimental platform outlined here differs from previous experiments in one key regard: the whole target assembly is embedded inside a pulsed magnetic-field generator (the 'magneto-inertial fusion electrical discharge system', or MIFEDS^{45,46}). When utilised, the MIFEDS generates a magnetic field with a magnitude of \sim 150 kG at the target foil and \sim 80 kG at the target's centre that is oriented approximately parallel to the axis which passes through the geometric centres of the foils and grids, and also along which both plasma jets propagate ('the line of centres'); Figure 1 shows a schematic of the magnetic field lines generated by the MIFEDS between the two grids. The magnitude of this magnetic field is significantly larger than that of the magnetic fields (~10 kG) generated by the Biermann battery and advected to the target's midpoint by the jets³⁸. However, the effect of a magnetic field of this strength on the dynamics of the interaction-region plasma is modest (as we explicitly demonstrate in sections III A and III B). Thus, this platform allowed us to test whether introducing a much larger seed magnetic field into the interactionregion plasma changes the magnitude of magnetic fields amplified by turbulent motions.

We characterised the turbulent plasma in both the presence and absence of the MIFEDS (which we refer to as 'MIFEDS experiments' and 'no-MIFEDS experiments', respectively) using three laser-plasma diagnostics: self-emission X-ray imaging to diagnose the plasma's dynamical evolution and turbulence, a time-resolved Thomson-scattering diagnostic to assess the plasma's physical state, and proton radiography using a D³He backlighter capsule to characterise magnetic fields. The set-up of all of these diagnostics was similar to that used in previous turbulent-dynamo experiments on the Omega Laser Facility³7,38, as was our methodology for analysing the data that was collected from them. However, for the sake of clarity and completeness, we provide a self-contained exposition here for each diagnostic that both reviews our approach and notes the aspects that are unique to this experiment.

III. RESULTS

A. Characterising turbulence: X-ray self-emission imaging

The X-ray imaging diagnostic measured soft X-rays (\sim 0.2-0.5 keV) emitted by free-free bremsstrahlung in the fully ionized CH plasma using a pinhole X-ray framing camera (XRFC) configured with a two-strip microchannel plate (MCP) and charged-coupled device (CCD) camera at a range of different times^{47,48}. The technical specifications of this XRFC were identical to that of the previous experiments³⁸; the magnification of the imaging was $2\times$, the pinhole diameter was 50 μ m, a thin filter (0.5 μ m polypropene with a 150 nm aluminium coating) was positioned in front of the MCP to block low-energy (\lesssim 0.1 keV) electromagnetic radiation, and each strip of the MCP was operated at two independent times, each with a 1 ns gate. The only difference with previous X-ray

imaging diagnostic set-ups was the orientation of the camera; in this experiment, the XRFC was oriented at a $\sim\!30^\circ$ angle with respect to the plane of the interaction-region plasma (60° with respect to the line of centres), in order to observe fluctuations in the plasma's emission within that plane. Previously, X-ray imaging was carried out in a side-on configuration (viz., at 90° with respect to the line of centres); however, on account of the interaction region's narrow extent with respect to the line of centres for a $\sim\!5$ ns interval subsequent to collision, detecting turbulent fluctuations during this time interval using this configuration proved to be challenging. XRFC images from the experiment both before and after the jet collision are shown in Figure 2.

Before the collision in both the MIFEDS and no-MIFEDS experiments (top row of Figure 2), we observe finger-like regions of emission from the plasma jets. Once the collision between these jets has occurred (second and subsequent rows of Figure 2) a region of strong, fluctuating emission (originating from the interaction-region plasma) develops. The fluctuations are related to density inhomogeneities in the plasma, whose origin can in turn be attributed to the effect of turbulent motions. Using a technique that was previously applied to similar X-ray imaging data³⁸, we can extract 'maps' of relative-intensity fluctuations for each of these post-collision images by first constructing a smooth mean X-ray intensity profile (for the technical details of the procedure, see the caption of Figure 3), and then dividing the total intensity by this profile; the resulting relative-intensity maps are shown in Figure 3.

Comparing the X-ray images obtained in the MIFEDS and no-MIFEDS experiments, we find the emission from the incident plasma jets to be slightly more extended and collimated in the former case (a physical explanation for this effect is provided with the help of Thomson scattering data in Section III B). However, once the interaction-region plasma has formed, the emission is qualitatively similar irrespective of whether the MIFEDS is turned on or not – this applies to both the size of the region from which X-rays are emitted and the fluctuations in the X-ray intensity.

To confirm these conclusions more robustly, we perform a quantitative analysis on the X-ray images. First, we measure the transverse extent l_i of the interaction-region plasma in both MIFEDS and no-MIFEDS experiments by averaging the same mean X-ray intensity profiles that we mentioned previously in the direction parallel to the line of centres, and then by calculating the full-width-half-maximum (FWHM) of the resulting one-dimensional profile. The results, which are presented in Figure 4a, show that l_i in both types of experiment is indeed indistinguishable within the error of the measurement. To show quantitatively that the statistical properties of the turbulence are not significantly affected by the presence of the MIFEDS, we use the fact that the interaction-region plasma is optically thin to its bremsstrahlung-dominated Xray emission³⁸ to relate the relative intensity fluctuations to path-integrated relative density fluctuations⁴⁹. Then, under the assumption of approximately isotropic and homogeneous density statistics (assumptions justified by previous analysis of similar experiments³⁸), we can determine the rms of rel-

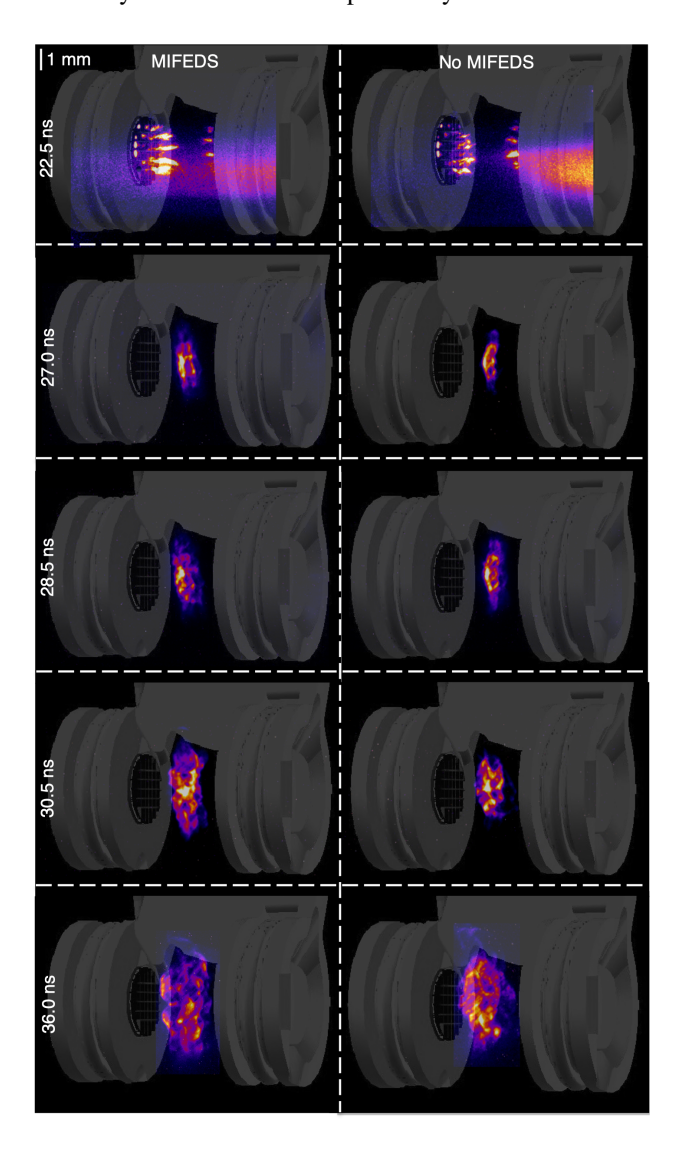


FIG. 2. X-ray self-emission images. XRFC images of soft X-rays emitted by the turbulent plasma in both the presence (left) and absence (right) of the MIFEDS. The top row (22.5 ns after the start of the drive-beam) employed a 100 V bias on the XFRC, while all other (post-collision) images used 350 V (the former having $32\times$ sensitivity). The resolution of the images, which is set by the pinhole size and the MCP's response, is $\sim 50~\mu m$. For reference, a projection of the target is shown on each image as a gray shade.

ative density fluctuations and their integral scale l_n . These quantities are shown in Figures 4b and 4c, respectively. The results are again similar for the MIFEDS and no-MIFEDS experiments, with one exception: the rms of relative density fluctuations not long after collision is larger in the presence of the MIFEDS magnetic field. We attribute this difference to a slightly earlier collision time in the MIFEDS experiments (see section III B) allowing for earlier onset of turbulent motions. The characteristic value (\sim 0.5) of the rms of relative density fluctuations in both the MIFEDS and no-MIFEDS experiments is close to values derived in previous experiments, as is the value of the integral scale l_n which is comparable to

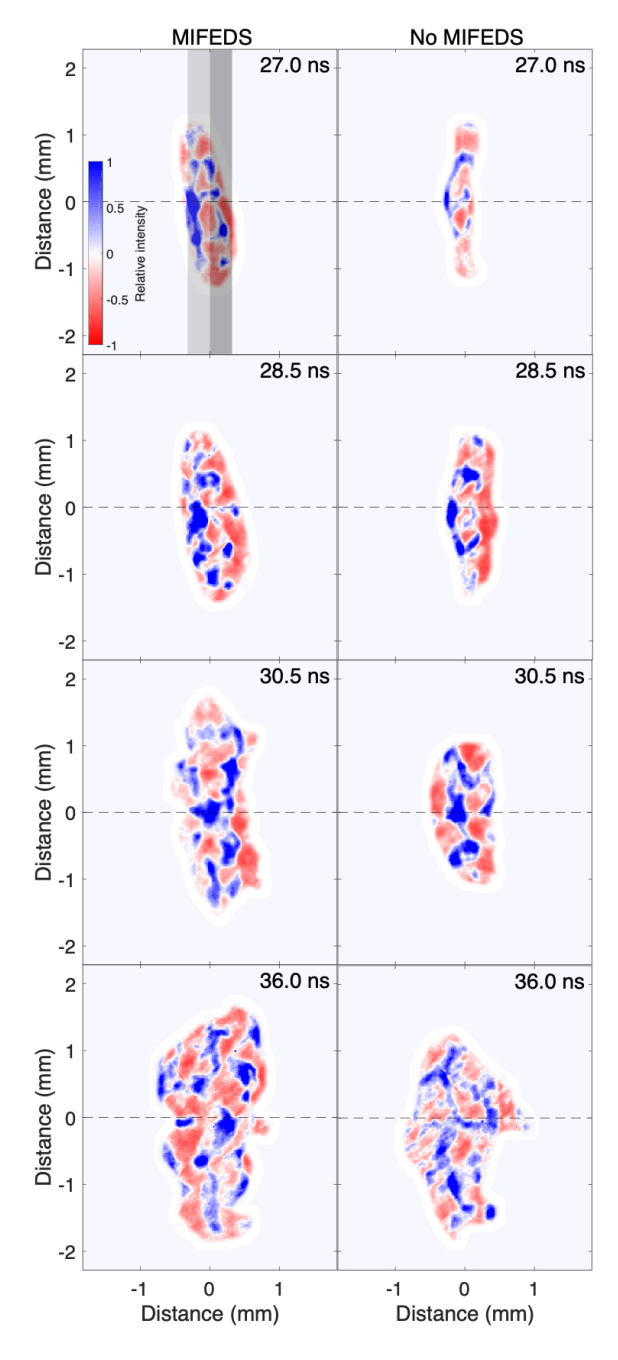


FIG. 3. Relative-intensity maps. Maps of fluctuations in the detected X-ray intensity relative to a smooth mean intensity profile. The mean profiles are determined from the raw data using a two-dimensional (2D) 81×81 pixel mean filter; given the effective 9 μ m pixel size of the images, this corresponds to a characteristic smoothing scale of \sim 0.8 mm (a value chosen to be intermediate between the transverse extent l_i of the interaction-region plasma and the grid periodicity L). This is then combined with a Gaussian-smoothed indicator function of the interaction-region plasma which has a characteristic smoothing scale of 150 μ m; this is equal to the characteristic length scale of the raw X-ray intensity profile in the direction parallel to the line of centres. The indicator function is utilised in order to account for the sharp drop in the measured X-ray intensity associated with the accretion shocks that circumscribe the interaction-region plasma. The gray shaded regions denote the intervals over which the mean X-ray intensity profile is averaged when determining l_i (see text).

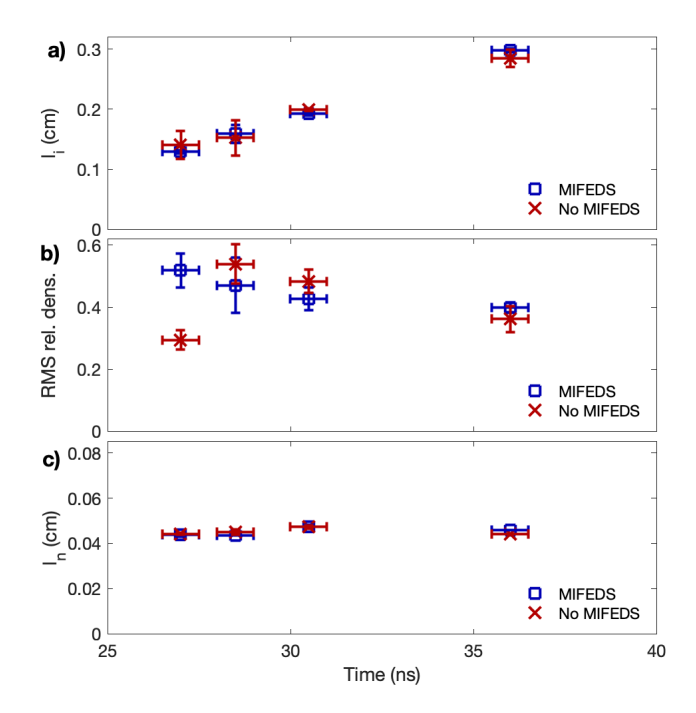


FIG. 4. Quantitative analysis of X-ray images. a) Evolution of the interaction-region transverse width l_i over time in the presence (blue squares) and absence (red crosses) of MIFEDS. The uncertainty of the measurement is estimated by assuming that the interaction-region plasma is approximately homogeneous, and then considering the left-hand and right-hand sides of the interaction region as independent samples (cf. Figure 3, top left panel). b) Evolution over time of the inferred rms magnitude of density fluctuations in the plasma. The uncertainty of the measurement is estimated in a similar manner to that described for a), but using the upper and lower regions of the interaction-region plasma instead of the left- and right-hand sides. c) Evolution over time of the inferred integral length l_n of density fluctuations in the plasma. The uncertainty is calculated in the same way as described for b). We note that our estimates of the rms of relative density fluctuations and l_n are not sensitive to the mean-filter length scale used to construct the mean X-ray intensity profile, provided it is chosen to be inside the interval $[L, l_i]$.

the grid periodicity L^{38} .

Under the same assumptions of statistical homogeneity and isotropy, we can also determine the spectrum of turbulent density fluctuations in the plasma. Since the turbulent motions are subsonic, density does not vary much $(\delta \rho/\bar{\rho} \sim 0.5)$ and behaves as a passive scalar: thus its spectrum is simply that of the turbulent velocity field⁵⁰. This property, which implies that the integral scale l_V of the turbulent velocity is approximately equal to that of the density $(l_V \approx l_n)$, was observed directly in a MHD FLASH simulation of similar (no-MIFEDS) experiments³⁸. The inferred turbulent spectra in these experiments, which are shown Figure 5, have a similar shape irrespective of both the time of the measurement and whether the MIFEDS magnetic field is present or not: the spectral peak is at a wavenumber $\sim 2\pi/L \approx 20 \text{ mm}^{-1}$, with spectra consistent with a Kolmogorov -5/3 power law at larger wavenumbers.

In summary, we conclude that while there are some modest differences in the plasma's initial dynamical evolution when

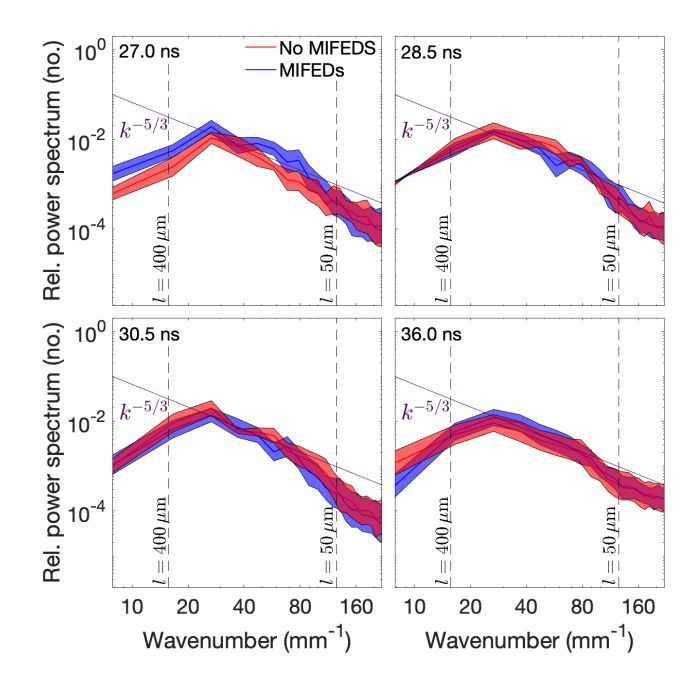


FIG. 5. Spectral analysis of relative X-ray intensity fluctuations. Inferred spectrum of density and velocity fluctuations in the plasma at four different times in the presence and absence of the MIFEDS magnetic field, respectively. We evaluate the (wavenumber-dependent) uncertainty of the measurement by combining the $\sim \! 10\%$ uncertainty associated with the signal-to-noise ratio of the X-ray images with the standard error in the inferred spectrum that arises when the upper and lower regions of the interaction-region plasma are treated as independent samples.

the MIFEDS is present, the key properties of the plasma turbulence in the interaction region are essentially unaffected by it.

B. Diagnosing the plasma's physical state: Thomson scattering

For the Thomson-scattering diagnostic employed in the experiment, a 30 J, green laser-probe beam (with wavelength 526.5 nm) was focused onto the centre of the target (and hence the centre of the interaction-region plasma), and scattered light collected at an angle of 63°. The orientation of the beam is shown in Figure 1. In this experiment, rather than carrying out measurements that were time-integrated over a 1 ns interval but spatially resolved along a 1.5 mm \times 50 μ m² cylindrical volume as was done previously³⁸, we instead performed time-resolved measurements in a 50 μ m³ volume over the 1 ns interval. To obtain time-resolved measurements over the complete evolution of the interactionregion plasma, we repeated the experiment but applied the Thomson-scattering probe beam at different times. For a selection of different times around (and after) the formation of the interaction-region plasma, the 'high-frequency' electronplasma-wave (EPW) feature was successfully measured on a spectrometer; this data are shown in Figure 6a. For rea-

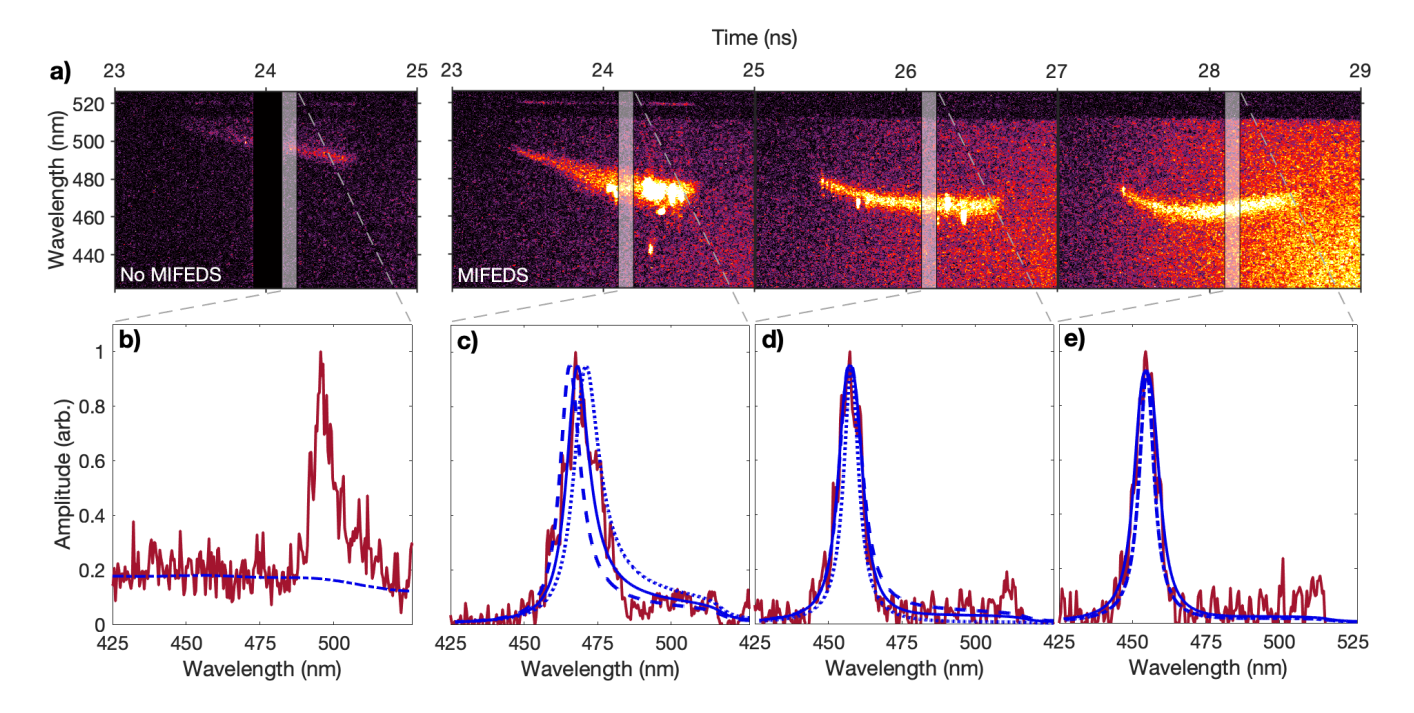


FIG. 6. Thomson-scattering data and fitting. a) Time-resolved EPW spectral features obtained in the experiment. Data were successfully collected for one shot without MIFEDS and three shots with MIFEDS. For the no-MIFEDS experiment (far-left panel), the spectrometer used to detect the EPW spectral feature gave an erroneous output for a 200 ps interval centred at 24.0 ns; this output has been masked in the panel. The absolute magnitude of the signals is normalised to the same value in each image. b) Plot of the experimental signal (solid red line) obtained from the raw data shown in the far-left panel of a) by averaging over an 100 ps interval centred at 24.15 ns (viz., the interval indicated by the white translucent region). The blue dot-dashed line indicates the fit to the background signal that we subtract prior to constructing a best-fit model to the EPW spectral feature. c) Plot of the experimental signal (with the background subtracted) obtained from the raw data shown in the mid-left panel of a) by averaging over an 100 ps interval centred at 24.15 ns, along with three possible spectral fits with different mean electron number densities: one with $\bar{n}_e = n_{e,\text{fit}} = 4.3 \times 10^{19} \, \text{cm}^{-3}$ (solid blue line), a second with $\bar{n}_e = 0.85n_{e,\text{fit}} = 3.6 \times 10^{19} \, \text{cm}^{-3}$ (dashed blue line). In all three cases, the assumed electron temperature (and mean electron number densities): one with $\bar{n}_e = n_{e,\text{fit}} = 7.9 \times 10^{19} \, \text{cm}^{-3}$ and $T_e = T_{e,\text{fit}} = 380 \, \text{eV}$ (solid blue line), one with $\bar{n}_e = 1.1n_{e,\text{fit}} = 8.7 \times 10^{19} \, \text{cm}^{-3}$ and $T_e = 0.5T_{e,\text{fit}} = 190 \, \text{eV}$ (dashed blue line), and one with $\bar{n}_e = 0.9n_{e,\text{fit}} = 7.1 \times 10^{19} \, \text{cm}^{-3}$ and $T_e = 1.5T_{e,\text{fit}} = 570 \, \text{eV}$ (dashed blue line). In all cases, a Gaussian spread of densities with $\Delta n_e/\bar{n}_e = 0.25 \, \text{was}$ assumed. e) Same as c), but at 28.15 ns, and with two possible spectral fits (both with $\bar{n}_e = n_{e,\text{fit}} = 8.8 \times 10^{19} \, \text{cm}^{-3}$ and $T_e = T_{e,\text{fit$

sons that remain uncertain, we were unable to detect successfully the low-frequency ion-acoustic-wave (IAW) feature; an anomalous signal saturated the spectrometer on which we had planned to detect this feature at the wavelengths over which it is typically observed.

We model the EPW feature using the well established theory of Thomson-scattering spectra that arise in plasmas⁵¹. In general, the Thomson-scattered spectrum $I(\mathbf{k}, \omega)$ at frequency ω of a laser probe beam with scattering wavevector \mathbf{k} is given by

$$I(\mathbf{k}, \boldsymbol{\omega}) = N_e I_0 \sigma_{\mathrm{T}} S(\mathbf{k}, \boldsymbol{\omega}), \qquad (1)$$

where N_e is the total number of electrons in the scattering volume, I_0 is the intensity of the incident laser probe, σ_T is the Thomson cross section for the scattering of a free electron, and $S(\mathbf{k}, \omega)$ is the dynamic form factor. We then adopt the Salpeter approximation for the form factor⁵¹, valid in a plasma with Maxwellian electron and ion distribution func-

tions whose electron and ion temperatures T_e and T_i and electron and ion number densities n_e and $n_i = n_e/Z$ (for Z the ion charge) are such that $\alpha \equiv 1/k\lambda_D \gg 1$, where λ_D is the Debye length. This is a reasonable assumption for the experimental conditions. In the Salpeter approximation,

$$S(\mathbf{k}, \omega) \approx \frac{1}{k \nu_{\text{the}}} \Gamma_{\alpha} \left(\frac{\omega - \omega_0}{k \nu_{\text{the}}} \right)$$
 (2)

at 'high' frequencies $\omega - \omega_0 \sim kv_{\text{th}e}$, where $v_{\text{th}e}$ is the thermal electron speed, ω_0 is the frequency of the incident laser probe,

$$\Gamma_{\alpha}(x) \equiv \frac{\exp\left(-x^2\right)}{\sqrt{\pi} \left[1 + \alpha^2 \left[1 + xZ(x)\right]\right]^2} \,,\tag{3}$$

and Z(x) is the plasma dispersion function⁵². It follows that the shape of the EPW spectral feature is directly related to n_e and T_e in a homogeneous plasma. Finally, in a turbulent plasma, the presence of density fluctuations in the interaction-

region plasma typically gives rise to a range of electron number densities within the scattering volume. To capture this effect, we therefore assume that n_e is isotropic and normally distributed in the scattering volume, with mean value \bar{n}_e and standard deviation Δn_e . The EPW feature can then be modelled by

$$S_{\mathrm{EPW}}(\mathbf{k}, \omega) \approx \frac{1}{\sqrt{\pi} \Delta n_e} \int \mathrm{d}\tilde{n}_e \exp\left[-\frac{(\tilde{n}_e - \bar{n}_e)^2}{\Delta n_e^2}\right] \times \frac{1}{k v_{\mathrm{th}e}} \Gamma_{\alpha} \left(\frac{\omega - \omega_0}{k v_{\mathrm{th}e}}\right).$$
 (4)

Qualitatively, for frequencies $\omega > \omega_0$, this feature has a single peak. The peak's position is sensitive to \bar{n}_e and, to a much lesser extent, to T_e , while its width is sensitive to T_e and Δn_e .

Having established a model for the EPW feature, we fit the data as follows. First, we perform a background subtraction in order to remove signals on the spectrometer that are unrelated to the EPW feature. The background signal is approximated using (Gaussian-filtered) samples taken just before and after the duration of the Thomson-scattering probe beam and then interpolating those signals to a given time (a typical background signal determined using this approach is shown in Figure 6b). Then, we fit equation (4) for particular choices of \bar{n}_e , T_e and Δn_e against 100-ps averaged samples of data, substituting for ω in terms of the wavelength λ using the dispersion relation $\omega = \omega(\lambda)$ of a light wave passing through a plasma. The approach of choosing \bar{n}_e , T_e and Δn_e differs depending on whether we are fitting EPW features close to the collision of the plasma jets, or subsequent to it. In the former case, we assume that turbulence has not yet developed and set $\Delta n_e = 0$; we then vary \bar{n}_e and T_e to obtain the best fit of the peak's position and width. In the latter case, we are faced with a degeneracy, with both changes in Δn_e and T_e having very similar effects on the width of the spectral peak. To overcome this degeneracy, we infer an estimate for Δn_e from the measurements of relative density fluctuations obtained using the X-ray imaging diagnostic (see section III A): namely, we assume that the rms of electron number density fluctuations on the scale $l_{\rm T}$ of the Thomson-scattering volume is related to the rms of electron number density fluctuations at the turbulence's integral scale via a Kolomogorov scaling $\Delta n_e/\bar{n}_e \approx (\Delta n_e/\bar{n}_e)_{l_n}(l_{\rm T}/l_n)^{1/3} \approx 0.25$. The validity of this assumption has been tested by our previous experiments³⁸, in which explicit measurements of $\Delta n_e/\bar{n}_e$ were made (possible due to successful simultaneous measurements of both the IAW and EPW features); these measurements indeed recovered similar values to those inferred from the X-ray images. We then once again adjust \bar{n}_e and T_e to give the best fit of the EPW spectral feature's position and width.

Once a best fit is obtained, we assess the sensitivity of the fits by first determining how the peak's position responds to changes in \bar{n}_e while keeping T_e fixed (see Figure 6c); next, we vary T_e and \bar{n}_e concurrently in such a way that the peak position remains fixed, but its width changes (see Figure 6d). We conclude from this analysis that the combined sensitivity of the fits to changes in n_e is $\pm 25\%$, while the sensitivity to changes in T_e is $\pm 50\%$ (taking correlated uncertainties into

account). Finally, the sensitivity of the fits to our assumptions concerning the magnitude of Δn_e is illustrated in Figure 6e; we find that, in the absence of any turbulent broadening, inferred electron temperatures would be $\sim 50\%$ larger. The mean electron number densities \bar{n}_e and temperatures T_e derived from the fitting procedure for all of the data are shown in Figure 7.

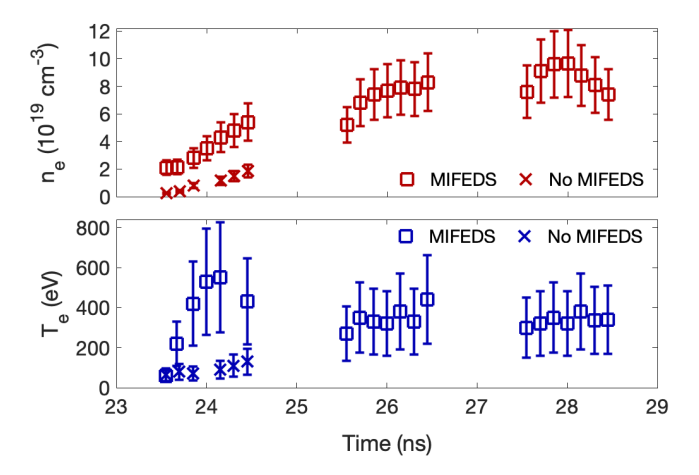


FIG. 7. Thomson-scattering derived measurements of the plasma's physical state. Evolution of the electron number density and temperature in the presence and absence of the MIFEDS magnetic field around and just after collision, as inferred from spectral fits. The uncertainties are determined from the sensitivity of the fits: $\pm 25\%$ for n_e , and $\pm 50\%$ for T_e . In the MIFEDS experiment, we were unable to construct a fit for the electron temperature at 24.3 ns on account of distortion of the EPW signal.

For the time interval of 23.5 ns to 24.5 ns during which we have data for both the MIFEDS and no MIFEDS experiments, we observe significant differences in the physical properties of the plasma: namely, the inferred values of n_e are much larger in the former case, and rapid heating of the electrons is observed in the presence of MIFEDS, but not in its absence. A compelling explanation for these observations is that the collision between the opposing plasma jets occurs ~ 1 ns earlier – at \sim 24 ns – in the MIFEDS experiments than in the no-MIFEDS experiments (in which collision occurs at \sim 25 ns based on prior measurements³⁸). The physical origin of this timing difference can be attributed to a dynamical collimation effect of the MIFEDS magnetic field on the jets. Using the data in Figure 7 to quantify the parameters of the jets just before they collide ($\rho_{\rm jet} \approx 6 \times 10^{-5}\,{\rm g/cm^3}, T_{e,\rm jet} \approx$ $T_{i,jet} \approx 100 \text{ eV}$), it follows that the characteristic kineticenergy density of the jets' transverse expansion (which we estimate as $\varepsilon_{\rm K,jet\perp}=\rho_{\rm jet}u_{\rm jet\perp}^2/2\approx 2.9\times 10^8~{\rm erg~cm^{-3}}$ by assuming that the expansion velocity $u_{\text{iet}\perp}$ is given by the sound speed $c_{\rm s} \approx 1.0 \times 10^7$ cm/s in the jet) is comparable to the magnetic-energy density $\varepsilon_{B_0} = B_0^2/8\pi \approx 2.5 \times 10^8$ erg ${\rm cm}^{-3}$ of the MIFEDS magnetic field. Therefore, the transverse expansion of the jets is at least partially inhibited by the MIFEDS magnetic field, a conclusion that is supported by the X-ray imaging observations (see Figure 2, top row). It is in turn plausible that this collimation is associated with a small increase in the jets' parallel velocity; the inferred collision timing difference is consistent with an \sim 5% increase in the initial jet velocities over the no-MIFEDS experiments to $u_{\rm jet}\approx 2.4\times 10^7$ cm/s. We note that, although the MIFEDS magnetic field does seem to have a dynamical effect on the plasma jets, the total characteristic kinetic-energy density of either jet ($\varepsilon_{\rm K,jet}=\rho_{\rm jet}u_{\rm jet}^2/2\approx 1.7\times 10^9$ erg) is indeed significantly larger than ε_{B_0} , as claimed in section II.

By contrast, the Thomson-scattering measurements of the interaction-region plasma's parameters in the MIFEDS experiments post collision are similar to those of no-MIFEDS experiments. A few ns after collision, we obtain characteristic temperatures $T_e \approx T_i \approx 250\text{-}450 \text{ eV}$, and electron number densities $n_e \approx (0.6\text{-}1.0) \times 10^{20} \, \text{cm}^{-3}$, parameters that are close to those inferred from previous experimental data collected on the Omega Laser Facility^{37,38}. While we do not have a direct measurement of the rms turbulent velocity in the MIFEDS experiments, the inferred \sim 5% difference in the incident jet velocities between the MIFEDS and no-MIFEDS experiments is small enough that, given the much larger \sim 40% uncertainty of the turbulent-velocity measurements in previous OMEGA experiments, we believe it to be reasonable to infer that the turbulent velocities in the no-MIFEDS and MIFEDS cases are similar ($u_{\rm rms} \approx 110$ km/s). Therefore, we conclude that a subsonic, turbulent plasma, with a turbulent Mach number of $\mathcal{M} \approx 0.5$ -0.7, a fluid Reynolds number of Rm ≈ 100 -900, and a (reasonably large) magnetic Reynolds number Rm ≈ 200-450, is indeed realized in this experiment⁵³, with that plasma's turbulent dynamics being affected minimally by the MIFEDS magnetic field. This latter conclusion is consistent with that derived from the X-ray imaging diagnostic.

C. Diagnosing the plasma's magnetic fields: proton radiography

The source of the protons for the proton-radiography diagnostic utilised in the experiment was a spherical aluminium-coated SiO₂ capsule (thickness 2 μ m, diameter 420 μ m) filled with 18 atm D³He gas, with the centre of the capsule located at a distance $r_s = 1$ cm away from the target's centre. This proton source has been carefully characterised in numerous prior studies^{54–56}. Upon irradiation with ~8 kJ of laser energy over a 1 ns interval, the capsule implodes in a few hundred picoseconds. D-D and D-³He nuclear fusion reactions, given by

$$D + D \rightarrow T[1.01 \text{ MeV}] + p[3.02 \text{ MeV}],$$
 (5)

$$D + {}^{3}He \rightarrow \alpha[3.6 \text{MeV}] + p[14.7 \text{MeV}],$$
 (6)

respectively, then generate $\sim 10^9~3.0~{\rm MeV}$ and 14.7 MeV protons over a $\sim 150~{\rm ps}$ interval centred $\sim 500~{\rm ps}$ after laser onset. Because of a net positive charge induced on the capsule during its implosion by laser irradiation, both proton species are accelerated by $\sim 300~{\rm keV}$ as they stream away from the capsule in all directions 56 . A fraction of these protons pass through the interaction-region plasma; the 15.0 MeV protons arrive $\sim 180~{\rm ps}$ after they are generated and transit through the plasma in $\sim 35~{\rm ps}$, while the equivalent times for the 3.3 MeV protons are $\sim 400~{\rm ps}$ and $\sim 80~{\rm ps}$, respectively. Both proton species subsequently reach a detector (located a distance $r_{\rm d}=27~{\rm cm}$

away from the target's centre) consisting of layers of the nuclear track detector CR-39 and metallic filters. The detector images the 3.3 and 15.0 MeV protons independently⁵⁴.

In contrast to previous Omega experiments investigating turbulent-dynamo processes, proton radiography in this experiment was performed in a side-on configuration with respect to the interaction-region plasma, in order to accommodate the change in orientation of the XRFC diagnostic. To obtain radiography measurements at different times, we repeated the experiments but changed the relative timing of the capsule implosion with respect to the drive beams incident on the CH foils

In our experiment, proton-radiography data provide a wealth of information about the magnetic fields encountered by the protons as they travel from the source to the detector. In the absence of any such fields, the proton-radiography beam would retain its inherent homogeneity, and thus the proton flux measured at the detector would be close to uniform. In reality, magnetic fields are encountered, and the action of Lorentz forces associated with these fields causes small deflections in the protons' trajectories, changing the location at which they arrive at the detector. In general laser-plasma experiments, electric fields could also cause these deflections; however, for laser-plasma dynamo experiments such as ours, their impact is minimal³⁷. If the proton beam is partially blocked prior to its interaction with the magnetic fields, deflections of the beam can be directly visualised, providing a very simple way to assess the path-integrated magnetic field. If the magnetic fields are also spatially heterogeneous, this can lead to significant transverse inhomogeneities in the proton beam as seen at the detector. Such inhomgeneities can be analysed quantitatively using a (now well established 37,38,40,57-60) technique that directly relates proton-flux inhomogeneities to the magnetic field path-integrated along the trajectory of the beam protons using a field-reconstruction algorithm^{61,62}; the technique is formally valid under a set of assumptions that are satisfied in the proton radiography set-up, and has been crossvalidated on the Omega Laser Facility using Faraday rotation measurements⁶³.

The proton-radiography diagnostic was first used to perform a calibration measurement of the MIFEDS-generated magnetic field, confirming that it has the expected strength and orientation. For this measurement, the MIFEDS was activated and the D³He capsule imploded, but the drive beams incident on the target's CH foils were not fired. The resulting 15.0-MeV and 3.3-MeV proton radiographs are shown in Figure 8. For a magnetic field that is oriented as indicated in Figure 1 (viz., approximately parallel to the line of centres), it is to be expected that the protons that pass through the centre of the target assembly would be displaced towards the left side of the detector, with the 3.3 MeV protons displaced further than 15.0 MeV protons. This is indeed what is observed in Figure 8: namely, before passing through the centre of the target assembly, part of both proton beams is blocked by a wire associated with the MIFEDS, and the apparent boundary of this wire is further on the left in the 3.3-MeV proton radiograph than in the 15.0-MeV radiograph.

More quantitatively, the path-integrated magnetic field ex-

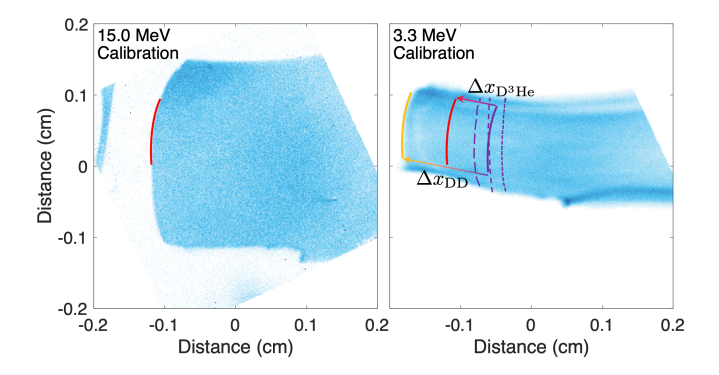


FIG. 8. Calibration measurement of the MIFEDS magnetic field with proton radiography. Left panel: 15.0-MeV proton radiograph of the target in the absence of any drive beams, but with MIFEDS on. The axes of the image, which has a ×28 magnification, are rescaled so that lengths are directly comparable with the plasma's scale. The reported pixel counts are normalised to their mean value (~60 protons/pixel) in a 0.1 cm by 0.1 cm square whose midpoint is at the centre of each image. Right panel: 3.3-MeV proton radiograph of same set-up. In both panels, the red line marks the apparent boundary of the 15.0 MeV proton beam, while the gold line marks the apparent boundary of the 3.3 MeV proton beam. The solid purple line marks the boundary of both proton beams in the absence of any magnetic fields that is inferred from the relative displacement of the apparent boundary of the 15.0 MeV and 3.3 MeV beams; the short-dashed, mid-dashed, and long-dashed lines denote the observed boundary of the 15.0 MeV proton beams at 25.2 ns, 31.2 and 38.7 ns, respectively, in the no-MIFEDS experiments. In these images, the line of centers is vertical and the targets and grids lie at the top and the bottom of it.

perienced by protons traversing the MIFEDS magnetic field can be explicitly estimated from the relative displacement of the boundary. In a point-projection radiography set-up, it can be shown⁶⁴ that the displacements $\Delta x_{\rm D^3He}$ and $\Delta x_{\rm DD}$ of protons from their undeflected position on the detector are given by $\Delta x_{\rm D^3He} \approx r_{\rm d}\Delta v_{\rm D^3He}/v_{\rm D^3He}$ and $\Delta x_{\rm DD} \approx r_{\rm d}\Delta v_{\rm DD}/v_{\rm DD}$, respectively (where $\Delta v_{\rm D^3He}$ and $\Delta v_{\rm DD}$ are the velocity perturbations of 15.0 MeV and 3.3 MeV protons acquired due to the interaction with the magnetic field, and $v_{\rm D^3He}$ and $v_{\rm DD}$ are the initial speeds of the 15.0 MeV and 3.3 MeV protons). In the limit of small deflections, $\Delta v_{\rm D^3He} \approx \Delta v_{\rm DD} \approx e \int B_{\perp} ds/m_p c$ is independent of the proton velocity (where B_{\perp} is the component of the magnetic field perpendicular to the direction of the proton beam, e is the elementary charge, e the speed of light, and e the proton mass), and so it follows that

$$\int B_{\perp} ds \approx \frac{m_p c v_{\text{D}^3 \text{He}} v_{\text{DD}}}{e(v_{\text{D}^3 \text{He}} - v_{\text{DD}})} \frac{\Delta x_{\text{DD}} - \Delta x_{\text{D}^3 \text{He}}}{r_{\text{d}}}.$$
 (7)

We find that $\Delta x_{\rm DD} - \Delta x_{\rm D^3 He} \approx 1.7$ cm; equation (7) then gives $\int B_{\perp} {\rm d}s \approx 25$ kG cm. This is consistent with theoretical expectations of the MIFEDS magnetic field, for which $B_{\perp} \approx 80$ kG across a region of extent $l_{\rm path} \approx 0.3$ cm. As a sanity check of the validity of this approach, in the right panel of Figure 8 we compare the position of the proton beam's undeflected boundary inferred from our calculation of $\int B_{\perp} {\rm d}s$ with direct measurements of this quantity in no-MIFEDS experiments (in which it is anticipated that the boundary of the proton beam is

unperturbed). We find reasonable agreement, given the uncertainties arising from the positioning of the MIFEDS wire due to inconsistent target fabrication.

Having calibrated the MIFEDS magnetic field strength and morphology, we then performed comparative measurements of magnetic fields arising in the turbulent interaction-region plasma with and without the MIFEDS switched on. 15.0 MeV proton radiographs recorded just after collision are shown in Figure 9, left column. It is clear that the inhomogeneities of

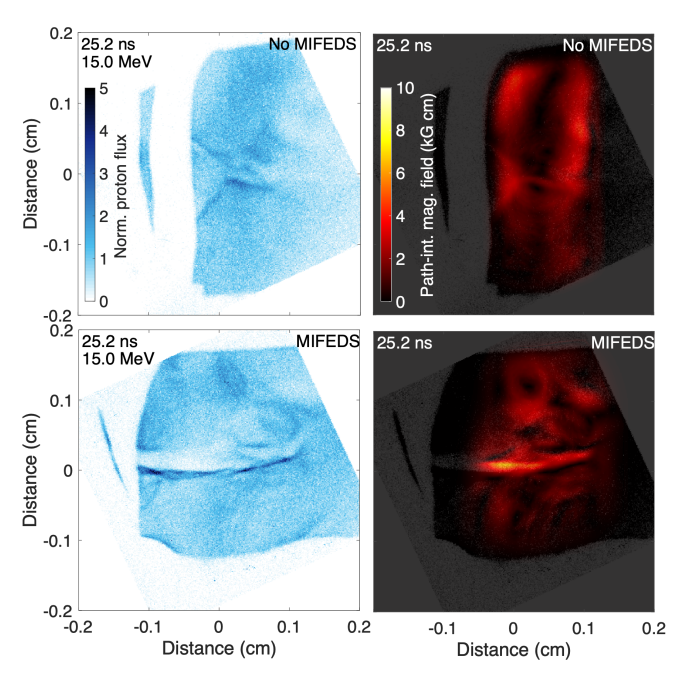


FIG. 9. Measurements of magnetic fields at collision with proton radiography. Left column: 15.0-MeV proton radiographs in the presence/absence of the MIFEDS at 25.2 ns (at a time close to the collision of the plasma jets). The pixel counts of each image are normalised to their mean value (\sim 60 protons/pixel) in a 0.1 cm by 0.1 cm square whose midpoint is at the centre of each image. In these images, the line of centers is vertical and the targets and grids lie at the top and the bottom of it. The location of the interaction region is offset by \sim 0.05 cm leftwards in the MIFEDS image due to the effect of the large-scale MIFEDS magnetic field. Right column: magnitude of the 'small-scale' components of the path-integrated magnetic field that is perpendicular to the trajectory of the proton radiography beam. In each case, we determine this quantity (using a field-reconstruction algorithm – see main text) over a region that is approximately coincident with the location of the interaction-region plasma, and only show those fluctuations in the path-integrated magnetic field whose characteristic scale is smaller than the characteristic size of the region analysed. In the case when the MIFEDS is on, we recover a largescale path-integrated magnetic field in addition to the small-scale path-integrated field that causes the deflection of protons leftwards that we discuss in the text. To enable direct comparison, this field is not shown, and the positioning of the small-scale path-integrated field in these cases is adjusted to take this deflection into account.

proton flux are more pronounced in the MIFEDS experiments than in the no-MIFEDS ones; because these inhomogeneities can be attributed to deflection of the proton beam by Lorentz forces associated with non-uniform magnetic fields present in the plasma⁶⁴, this implies stronger seed fields. 2D maps of the path-integrated magnetic field reconstructed using a field-reconstruction algorithm⁶¹ are shown in Figure 9, right column; when the MIFEDS is on, we estimate that the initial magnetic-field strength in the interaction-region plasma is

$$B_0 \approx 60 \left[\frac{\int B_{\perp} ds}{6 \,\mathrm{kGcm}} \right] \left[\frac{l_{\mathrm{path}}}{0.1 \,\mathrm{cm}} \right]^{-1} \mathrm{kG},$$
 (8)

(where l_{path} is the path-length of the protons through the interaction-region plasma). This value is comparable to (though not the same as) the MIFEDS field in the absence of the plasma jets, and is also much larger than the Biermann battery-generated seed fields observed in no-MIFEDS experiments ($B_0 \approx 10$ kG). The difference between the strength (and also the morphology) of the measured seed field in the MIFEDS experiment at the time of collision and the MIFEDS field in the absence of the interaction-region plasma is most plausibly explained by the interaction of the plasma jets with the MIFEDS field; the former's kinetic-energy density is approximately ten times greater than the magnetic-energy density of the MIFEDS magnetic fields, and the jets' magnetic Reynolds number is significantly larger than unity ($Rm_{iet} \approx$ 50-90), which results in the MIFEDS magnetic field being advected with the plasma jets as they expand towards each other.

In contrast to our findings close to the jet collision, both the (stochastic) proton-flux inhomogeneities and the reconstructed path-integrated magnetic fields are much more similar over one driving-scale turbulent eddy-turnover time (\sim 6 ns) after collision (see Figure 10), and also over three drivingscale eddy-turnover times (\sim 13.5 ns) after the collision (see Figure 11). Qualitatively, the proton radiographs from the MIFEDS and no-MIFEDS experiments are not completely identical: a significant proton-flux inhomogeneity with a magnitude much greater than the mean proton flux of the image, which is associated with the interaction of the MIFEDS field with the edge of the interaction-region plasma, is evident in the former on the right of the radiograph. However, the stochastic proton-flux inhomogeneities in the centre of the interaction-region plasma are much harder to distinguish, as are the stochastic path-integrated fields. Assuming that the magnetic field has isotropic and homogeneous statistics, we estimate the rms magnetic-field strength $B_{\rm rms}$ from the path-integrated magnetic-field maps via the relation $B_{\rm rms} pprox \int B_{\perp} {
m d}s / \sqrt{\ell_B l_{
m path}}$ (where ℓ_B is the field's correlation length)61. For both the MIFEDS and no-MIFEDS experiments \sim 6 ns after collision, we obtain

$$B_{\rm rms} \approx 100 \left[\frac{\int B_{\perp} ds}{4.5 \,\mathrm{kG\,cm}} \right] \left[\frac{\ell_B}{0.01 \,\mathrm{cm}} \right]^{-1/2} \left[\frac{l_{\rm path}}{0.2 \,\mathrm{cm}} \right]^{-1/2} \mathrm{kG}.$$

This is comparable to the measured values of $B_{\rm rms}$ in previous experiments with similar Rm^{37,38}. We can also estimate the magnetic-energy spectrum via the relation

$$E_B(k) = \frac{1}{4\pi^2 l_{\text{path}}} k E_{\text{path}}(k), \qquad (10)$$

where $E_{\text{path}}(k)$ is the spectrum of the path-integrated magnetic fields; we note that the effective resolution of the proton-

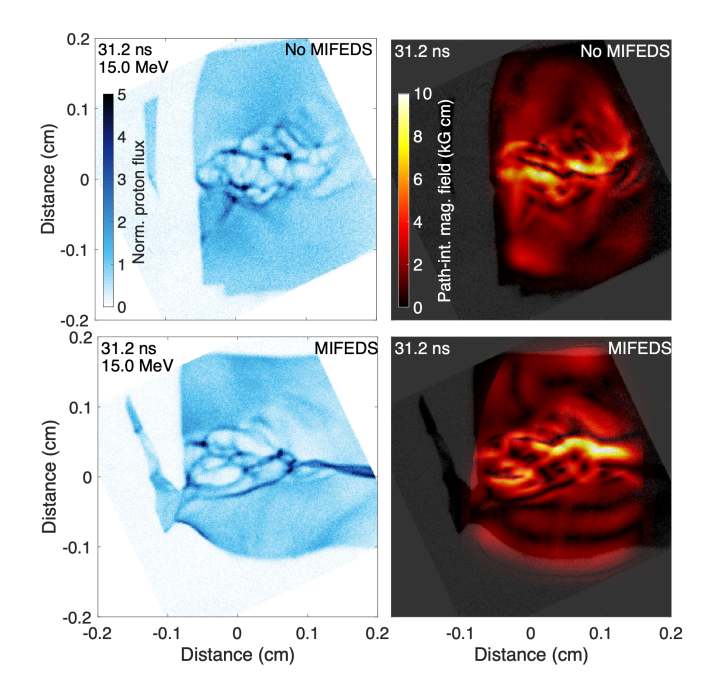


FIG. 10. Measurements of magnetic fields post collision with proton radiography. Left column: 15.0-MeV proton radiographs in the presence/absence of the MIFEDS \sim 6 ns after collision. Each image is normalised to its mean value (\sim 60 protons/pixel) in a 0.1 cm by 0.1 cm area in the centre of each image. In these images, the line of centers is vertical and the targets and grids lie at the top and the bottom of it. The location of the interaction region is offset by \sim 0.05 cm leftwards in the MIFEDS image due to the effect of the large-scale MIFEDS magnetic field. The long horizontal feature in the MIFEDS image lies to the right of the interaction region (see text). Right column: magnitude of the small-scale components of the (perpendicular) path-integrated magnetic field.

radiography diagnostic is \sim 100-200 μ m, so we only obtain the spectrum of the fields whose scale is comparable to the integral scale l_n of the turbulence. The magnetic-energy spectra for both MIFEDS and no-MIFEDS experiments at 31.2 ns are shown in Figure 12, left panel; within the uncertainty of the measurement, they are the same. The similarity of the magnetic field's strength and morphology between the MIFEDS and no-MIFEDS experiments is also evident in the proton-radiography data, reconstructed path-integrated magnetic fields, and magnetic-energy spectra obtained at the later times (see Figure 12, right panel). Intriguingly, even though the correlation length is similar, the characteristic value of the rms magnetic-field strength is somewhat reduced at late times compared to earlier ones in both MIFEDS and no-MIFEDS experiments: $B_{\rm rms} \approx 50$ kG at 38.7 ns (as compared with $B_{\rm rms} \approx 100 \; {\rm kG}$ at 31.2 ns). A plausible explanation for this observation is the decay of the turbulent kinetic energy by this stage of the interaction-region plasma's evolution (which has been seen in simulations of similar experiments³⁸).

In summary, the proton radiography data confirm that the magnetic field in the interaction-region plasma postamplification is not significantly altered by the MIFEDS in spite of much stronger seed magnetic fields and somewhat dis-

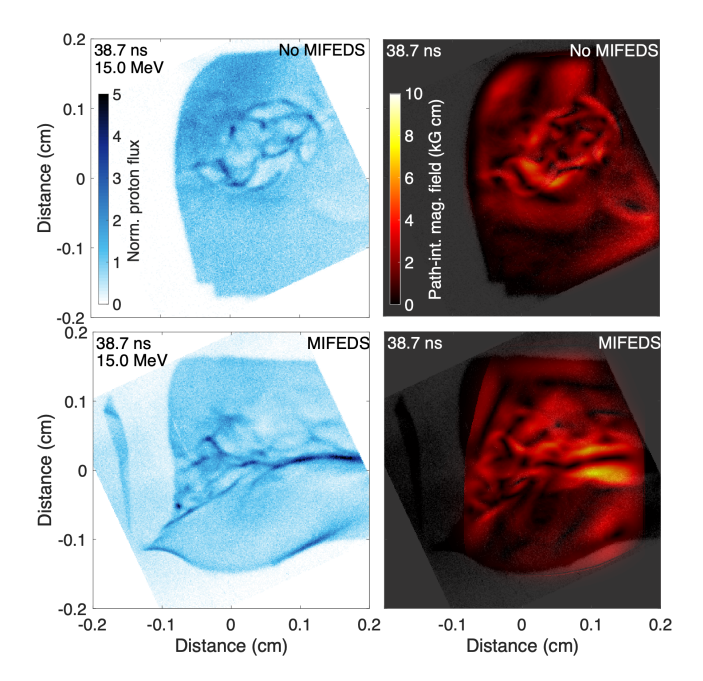


FIG. 11. Measurements of magnetic fields at late times with proton radiography. Left column: 15.0-MeV proton radiographs in the presence/absence of the MIFEDS 13.5 ns after collision. The proton flux is detected using a CR-39 detector stack. The pixel counts of each image are normalised to their mean value (\sim 60 protons/pixel) in a 0.1 cm by 0.1 cm square whose midpoint is at the centre of each image. In these images, the line of centers is vertical and the targets and grids lie at the top and the bottom of it. The location of the interaction region is offset by \sim 0.05 cm leftwards in the MIFEDS image due to the effect of the large-scale MIFEDS magnetic field. The long horizontal feature in the MIFEDS image lies to the right of the interaction region (see text). Right column: magnitude of the small-scale components of the (perpendicular) path-integrated magnetic field.

tinct initial flow dynamics in the interaction-region plasma.

IV. DISCUSSION

In the experiments described above, we have found that using MIFEDS to introduce a magnetic seed field ($B_0 \approx 60 \, \text{kG}$) into a turbulent, Rm-supercritical laser-plasma that is six times larger than the inherent seed field self-generated by the Biermann battery does not lead to larger values of B_{rms} postamplification; instead, the same value ($B_{\text{rms}} \approx 100 \, \text{kG}$) is measured in both MIFEDS and no-MIFEDS experiments (see Section III C). Further, the statistics of the amplified magnetic fields arising in both types of experiments could not be distinguished. This result was attained despite the MIFEDS seed field being strong enough to modify (somewhat) the dynamics of the counter-propagating jets that form the turbulent plasma on their collision (see Section III A).

One immediate corollary of this finding is that the amplified magnetic field in the turbulent plasma must be dynamically significant. In resistive MHD, which is a reasonable model for the collisional CH laser-plasmas present in the experiment, the evolution of a dynamically insignificant field is linear, and

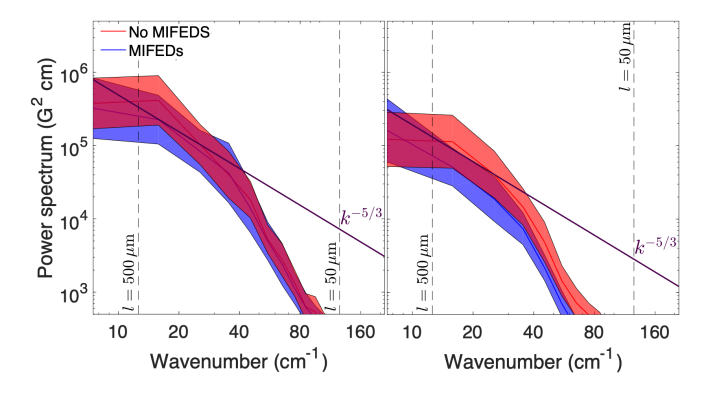


FIG. 12. Measurements of magnetic-energy spectra using proton radiography. Magnetic-energy spectra inferred from proton radiography data under the assumption of homogeneous and isotropic stochastic magnetic fields. Spectra obtained from no-MIFEDS experiments are shown in red, and those from MIFEDS experiments in blue. The nominal limit on the resolution due to the finite size of the proton source is indicated on each plot; however, the actual resolution scale is observed to be a few times larger than indicated due to a systematic blurring of the proton-radiography data that stems from self-intersection of the proton beam prior to its detection (the selfintersection is caused by small-scale stochastic magnetic fields in the plasma^{40,61}). The uncertainty of the measurement of the spectrum is estimated by assuming that the interaction-region plasma is homogeneous, and then treating the interaction region's left- and right-hand sides as independent samples. Left panel: magnetic-energy spectra at 31.2 ns after collision. Right panel: magnetic-energy spectra at 38.7 ns.

thus is proportional to B_0 . We conclude that $B_{\rm rms}$ cannot be dynamically insignificant with respect to turbulent motions in the interaction-region plasma, because if it were so, then introducing the larger seed field using the MIFEDS would have resulted in larger magnetic field strengths post-amplification. This result is perhaps surprising, given the value of the magnetic to turbulent-kinetic energy ratio is only $\varepsilon_{\rm B}/\varepsilon_{\rm K,turb} \approx 3\%$. However, periodic-box MHD simulations of the small-scale (subsonic) turbulent dynamo with similar Rm and Pm values in which back-reaction can be explicitly identified have found that, in fact, the magnetic field begins to back-react on the turbulent motions once $\varepsilon_{\rm B}/\varepsilon_{\rm K,turb} \gtrsim 1\%^{19}$.

Our result that the strength and structure of dynamically significant dynamo-amplified magnetic fields is not sensitive to the strength of the initial seed fields is generally consistent with the results of periodic-box MHD simulations of the small-scale turbulent dynamo. For example, one recent study of this type²⁸ found that the characteristic values of $B_{\rm rms}$, the correlation length l_B and the magnetic-energy spectrum E_B in the saturated state of a turbulent dynamo (with Rm = 2000, Pm = 1, and $\mathcal{M} = 0.1$) were indistinguishable for two different seed-field strengths ($\varepsilon_{\rm B}/\varepsilon_{\rm K,turb}(t=0)\approx 8\times 10^{-10}$ and $\varepsilon_{\rm B}/\varepsilon_{\rm K,turb}(t=0)\approx 8\times 10^{-12}$, respectively), and also three qualitatively distinct seed magnetic-energy spectra. That being said, the initial seed-field strengths in these simulations were much smaller than were present in the experiment, and the authors are not aware of any periodic-box simulations that are more directly comparable in terms of parameters and also

investigated the role of seed fields on the dynamo.

The \sim 3% value of the magnetic-to-kinetic energy ratio we observed, which is consistent with the maximum values of this quantity seen in earlier comparable laboratory experiments^{37,38}, merits further discussion. It was previously noted³⁸ that the saturation values of $\varepsilon_{\rm B}/\varepsilon_{\rm K,turb}$ in periodicbox simulations of the subsonic small-scale turbulent dynamo at comparable Rm and Pm tend to be somewhat larger $(\varepsilon_{\rm B}/\varepsilon_{\rm K,turb} \approx 8\%^{13,19})$ than the reported experimental values. One explanation for this discrepancy is that the field growth has fully saturated in the experiments at a smaller energy ratio because the turbulent flow itself is qualitatively different from that in periodic-box simulations. These differences include the interaction-region plasma in the experiment not being fully incompressible (which is predicted theoretically to alter the saturation value^{65,66}) and also not spatially homogeneous and periodic; in the latter regard, strong shear flows in the interaction-region plasma in addition to turbulent motions were identified³⁸ in MHD simulations of a previous experiment completed using FLASH. Another (previously proposed³⁸) explanation for this discrepancy was that an insufficient number of driving-scale eddy-turnover times had passed in the experiments for the dynamo to have saturated.

In light of the new results reported in this paper, the latter of the two explanations might seem untenable, as it would require identical transient magnetic-field strengths to be reached starting with two different seed fields over the same period of time. However, this explanation cannot, in fact, be ruled out or corroborated by our new experimental results. This is because the initial field in the MIFEDS experiment ($B_0 \approx 60 \text{kG}$), while larger than in the no-MIFEDS one ($B_0 \approx 10 \, \text{kG}$), is still small enough for its amplification to start in the kinematic phase of dynamo action; in both experiments, the magnetic field first grows exponentially fast at a rate γ_{kin} to a dynamical strength $B_{\rm nl}$ over a very short time $(t_{\rm kin})$, and then spends most of the time being amplified further in the nonlinear, secular regime. It is then natural that measurements at a time interval $\Delta t \sim 6$ ns $\gg t_{\rm kin}$ after the jet collision would find the same state. Based on previous time-resolved measurements of the magnetic field³⁸, we estimate that $\gamma_{kin} \sim 1.8 \times 10^9 \, s^{-1}$, $B_{\rm nl} \sim 86$ kG, and so $t_{\rm kin} \sim 1.2$ ns $(\Delta t - t_{\rm kin} \sim 4.8$ ns) in the no-MIFEDS experiments and $t_{\rm kin} \sim 0.2 \, \rm ns$, ($\Delta t - t_{\rm kin} \sim 5.8 \, \rm ns$) in the MIFEDS ones. In both cases, $\Delta t - t_{kin}$ is comparable to \sim 1-2 driving-scale eddy turnover times $\tau_{\rm eddy}$ (\sim 4 ns). Assuming that periodic-box simulations are applicable, saturation of the dynamo in them takes $\sim 3-5\tau_{\rm eddy}$ after the beginning of the nonlinear dynamo regime — a somewhat longer period than our experiment lasts. We therefore remain uncertain about whether the dynamo has fully saturated in these experiments.

This conclusion clearly points towards the most pressing future direction for laser-plasma experiments investigating the small-scale turbulent dynamo: more experiments with time-resolved measurements over a longer period and/or with larger seed fields, closer to the current level achieved at the end of the experiment. Only then will it possible to confirm definitively whether the dynamo in the experiments has saturated. An experimental programme of this sort would have other tangible benefits too. For example, time-resolved proton-

radiography measurements with a shorter interval spacing made of the MIFEDS experiments (as has already been made in no-MIFEDS experiments³⁸) would allow for a more detailed comparison of key properties of the magnetic field (including some not measurable from our current data e.g. the field's growth rate). If such measurements were successfully made just after the interaction-region plasma's formation, it might also be possible to determine directly the initial spectrum of seed magnetic fields on which the turbulent dynamo acts directly. Such a measurement would extend our results if this spectrum differed between MIFEDS and no-MIFEDS experiments.

In summary, our results support a key prediction of theoretical dynamo theory: that, in a turbulent, magnetised fluid, changing the initial seed field's strength (and also modestly changing the initial conditions of the turbulence) does not lead to larger characteristic magnetic-field strengths postamplification. More generally, it also suggests that in turbulent, Rm-supercritical plasmas, magnetic fields will tend to undergo quasi-spontaneous amplification, and become dvnamically significant. In addition to astrophysical applications already discussed in the Introduction, this conclusion is also relevant to inertial-confinement fusion (ICF) experiments. More specifically, if turbulence-generating fluid instabilities such as the Rayleigh-Taylor instability are also present in ICF implosions, and high enough plasma temperatures are attained to realise Rm supercriticality, it is possible that Biermann-battery fields self-generated during those implosions could be further amplified⁶⁷. If these fields become strong enough to magnetise the ICF plasma's electron species (viz., bring the Hall parameter to order unity), the plasma's electron thermal conductivity is altered significantly^{68,69}, in turn affecting key metrics such as ion temperature and neutron yield; such an effect has been reported in 3D extended-MHD simulations of the stagnation phase of an indirect-drive implosion on the National Ignition Facility⁷⁰. If magnetic fields also attain dynamical strengths post-amplification, the back-reaction of those fields on turbulence will tend to suppress inertial-range turbulent motions¹³, in turn reducing turbulent mixing in imploded ICF plasmas. Such considerations are particularly prescient in the case of magnetised ICF efforts that aim to leverage strong pre-imposed magnetic fields to control heat transport⁷¹, because the degree of amplification required before magnetic fields become important will be lessened.

ACKNOWLEDGMENTS

The research leading to these results has received funding from the European Research Council under the European Community's Seventh Framework Programme (FP7/2007-2013)/ERC grant agreements no. 256973 and 247039, the U.S. Department of Energy (DOE) National Nuclear Security Administration (NNSA) under Contract No. B591485 to Lawrence Livermore National Laboratory (LLNL), Field Work Proposal No. 57789 to Argonne National Laboratory (ANL), Subcontracts No. 536203 and 630138 with

Los Alamos National Laboratory, Subcontract B632670 with LLNL, and grants No. DE-NA0002724, DE-NA0003605, and DE-NA0003934 to the Flash Center for Computational Science, DE-NA0003868 to the Massachusetts Institute of Technology, and Cooperative Agreement DE-NA0003856 to the Laboratory for Laser Energetics University of Rochester. We acknowledge support from the U.S. DOE Office of Science Fusion Energy Sciences under grant No. SC0016566 and the National Science Foundation under grants No. PHY-1619573, PHY-2033925 and PHY-2045718. We acknowledge funding from grants 2016R1A5A1013277 and 2020R1A2C2102800 of the National Research Foundation of Korea. Support from AWE plc., the Engineering and Physical Sciences Research Council (grant numbers EP/M022331/1, EP/N014472/1, and EP/R034737/1) and the U.K. Science and Technology Facilities Council is also acknowledged. The authors thank General Atomics for target manufacturing and R&D support, funded by the U.S. DOE NNSA in support of the NLUF program through subcontracts 89233118CNA000010 and 89233119CNA000063.

DATA AVAILABILITY STATEMENT

The data that support the findings of this study are available from the corresponding author upon reasonable request.

- ¹L. Biermann and A. Schluter, "Cosmic radiation and cosmic magnetic fields: II. Origin of cosmic magnetic fields," Phys. Rev. **29**, 29 (1951).
- ²V. Vacca, M. Murgia, F. Govoni, T. Enßlin, N. Oppermann, L. Feretti, G. Giovannini, and F. Loi, "Magnetic fields in galaxy clusters and in the large-scale structure of the universe," Galaxies **6**, 142 (2018).
- ³G. K. Batchelor, "On the spontaneous magnetic field in a conducting liquid in turbulent motion," Proc. R. Soc. A **201**, 405 (1950).
- ⁴D. Ryu, H. Kang, J. Cho, and S. Das, "Turbulence and magnetic fields in the large-scale structure of the universe," Science **320**, 909 (2008).
- ⁵A. Kazantsev, "Enhancement of a magnetic field by a conducting fluid," Soviet-JETP 26, 1031 (1968).
- ⁶S. I. Vainstein and Y. B. Zel'dovich, "Review of topical problems: origin of magnetic fields in astrophysics (turbulent 'dynamo' mechanisms)," Sov. Phys. Usp. **15**, 159 (1972).
- ⁷Y. B. Zel'dovich, A. A. Ruzmaikin, S. A. Molchanov, and D. D. Sololov, "Kinematic dynamo problem in a linear velocity field," J. Fluid Mech. **144**, 1 (1984).
- ⁸R. Kulsrud and S. W. Anderson, "The spectrum of random magnetic fields in the mean field dynamo theory of the galactic magnetic field," Astrophys. J. 396, 606 (1992).
- ⁹M. Meneguzzi, U. Frisch, and A. Pouquet, "Helical and nonhelical turbulent dynamos," Phys. Rev. Lett. **47**, 1060 (1981).
- ¹⁰S. Kida, S. Yanase, and J. Mizushima, "Statistical properties of mhd turbulence and turbulent dynamo," Phys. Fluids A 3, 457 (1991).
- ¹¹R. S. Miller, F. Mashayek, V. Adumitroaie, and P. Givi, "Structure of homogeneous nonhelical magnetohydrodynamic turbulence," Phys. Plasmas 3, 3304 (1996).
- ¹²J. Cho and E. T. Vishniac, "The generation of magnetic fields through driven turbulence," Astrophys. J. **538**, 217 (2001).
- ¹³ A. A. Schekochihin, S. C. Cowley, S. F. Taylor, J. L. Maron, and J. C. McWilliams, "Simulations of the small-scale turbulent dynamo," Astrophys. J. 612, 276 (2004).
- ¹⁴N. E. Haugen, A. Brandenburg, and W. Dobler, "Simulations of nonhelical hydromagnetic turbulence," Phys. Rev. E 70, 016308 (2004).
- ¹⁵ A. A. Schekochihin, A. B. Iskakov, S. C. Cowley, J. C. McWilliams, M. R. E. Proctor, and T. A. Yousef, "Fluctuation dynamo and turbulent induction at low magnetic prandtl numbers," New J. Phys. 9, 300 (2007).

- ¹⁶J. Cho and D. Ryu, "Characteristic lengths of magnetic field in magnetohy-drodynamic turbulence," Astrophys. J. 705, L90 (2009).
- ¹⁷A. Beresnyak, "Universal nonlinear small-scale dynamo," Phys. Rev. Lett. 108, 035002 (2012).
- ¹⁸D. H. Porter, T. W. Jones, and D. Ryu, "Vorticity, shocks, and magnetic fields in subsonic, icm-like turbulence gas motions in the intra-cluster medium," Astrophys. J. 810, 93 (2015).
- ¹⁹A. Seta, P. J. Bushby, A. Shukurov, and T. S. Wood, "On the saturation mechanism of the fluctuation dynamo at Pm > 1," Phys. Rev. Fluids 5, 043702 (2020).
- ²⁰F. Rincon, "Dynamo theories," J. Plasma Phys. **85**, 205850401 (2019).
- ²¹D. A. St-Onge, M. W. Kunz, J. Squire, and A. A. Schekochihin, "Fluctuation dynamo in a weakly collisional plasma," J. Plasma Phys. 86, 905860503 (2020).
- ²²A. Seta and C. Federrath, "Saturation mechanism of the fluctuation dynamo in supersonic turbulent plasmas," Phys. Rev. Fluids 6, 103701 (2021).
- ²³C. L. Carilli and G. B. Taylor, "Cluster magnetic fields," Annu. Rev. Astron. Astrophys. 40, 319 (2002).
- ²⁴F. Govoni and L. Feretti, "Magnetic fields in clusters of galaxies," Int. J. Mod. Phys. D 13, 1549 (2004).
- ²⁵R. Beck, "Magnetic fields in spiral galaxies," Astron. Astrophys. Rev. 24, 4 (2016).
- ²⁶R. M. Kulsrud, R. Cen, J. P. Ostriker, and D. Ryu, "The protogalactic origin for cosmic magnetic fields," Astrophys. J. 480, 481 (1997).
- ²⁷P. Bhat and K. Subramanian, "Fluctuation dynamo at finite correlation times and the kazantsev spectrum," Astrophys. J. Lett. **791**, L34 (2014).
- ²⁸A. Seta and C. Federrath, "Seed magnetic fields in turbulent small-scale dynamos," Mon. Not. R. Astron. Soc. **499**, 2076 (2020).
- ²⁹ A. Gailitis, O. Lielausis, S. Dement'ev, E. Platacis, A. Cifersons, G. Gerbeth, T. Gundrum, F. Stefani, M. Christen, H. Hänel, and G. Will, "Detection of a flow induced magnetic field eigenmode in the riga dynamo facility," Phys. Rev. Lett. 84, 4365 (2000).
- ³⁰ A. Gailitis, O. Lielausis, E. Platacis, S. Dement'ev, A. Cifersons, G. Gerbeth, T. Gundrum, F. Stefani, M. Christen, and G. Will, "Magnetic field saturation in the riga dynamo experiment," Phys. Rev. Lett. 86, 3024 (2001).
- ³¹R. Monchaux, M. Berhanu, M. Bourgoin, M. Moulin, P. Odier, J.-F. Pinton, R. Volk, S. Fauve, N. Mordant, F. Pétrélis, A. Chiffaudel, F. Daviaud, B. Dubrulle, C. Gasquet, L. Marié, and F. Ravelet, "Generation of a magnetic field by dynamo action in a turbulent flow of liquid sodium," Phys. Rev. Lett. 98, 044502 (2007).
- ³²G. Gregori, A. Ravasio, C. D. Murphy, K. Schaar, A. Baird, A. R. Bell, A. Benuzzi-Mounaix, R. Bingham, C. Constantin, R. P. Drake, M. Edwards, E. T. Everson, C. D. Gregory, Y. Kuramitsu, W. Lau, J. Mithen, C. Niemann, H.-S. Park, B. A. Remington, B. Reville, A. P. L. Robinson, D. D. Ryutov, Y. Sakawa, S. Yang, N. C. Woolsey, M. Koenig, and F. Miniati, "Generation of scaled protogalactic seed magnetic fields in laser-produced shock waves." Nature 481, 480 (2012).
- ³³J. Meinecke, H. W. Doyle, F. Miniati, A. R. Bell, R. Bingham, R. Crowston, R. P. Drake, M. Fatenejad, M. Koenig, Y. Kuramitsu, C. C. Kuranz, D. Q. Lamb, D. Lee, M. J. MacDonald, C. D. Murphy, H.-S. Park, A. Pelka, A. Ravasio, Y. Sakawa, A. A. Schekochihin, A. Scopatz, P. Tzeferacos, W. C. Wan, N. C. Woolsey, R. Yurchak, B. Reville, and G. Gregori, "Turbulent amplification of magnetic fields in laboratory laser-produced shock waves," Nat. Phys. 10, 520 (2014).
- ³⁴J. Meinecke, P. Tzeferacos, A. Bell, R. Bingham, R. Clarke, E. Churazov, R. Crowston, H. Doyle, R. P. Drake, R. Heathcote, M. Koenig, Y. Kuramitsu, C. Kuranz, D. Lee, M. MacDonald, C. Murphy, M. Notley, H. Park, A. Pelka, A. Ravasio, B. Reville, Y. Sakawa, W. Wan, N. Woolsey, R. Yurchak, F. Miniati, A. Schekochihin, D. Lamb, and G. Gregori, "Developed turbulence and nonlinear amplification of magnetic fields in laboratory and astrophysical plasmas," Proc. Natl. Acad. Sci. U.S.A. 112, 8211 (2015).
- ³⁵G. Gregori, B. Reville, and F. Miniati, "The generation and amplification of intergalactic magnetic fields in analogue laboratory experiments with high power lasers," Phys. Rep. 601, 1 (2015).
- ³⁶P. Tzeferacos, A. Rigby, A. F. A. Bott, A. R. Bell, R. Bingham, F. Cattaneo, E. M. Churazov, F. Fiuza, C. Forest, J. Foster, C. Graziani, J. Katz, M. Koenig, C.-K. Li, J. Meinecke, R. Petrasso, H.-S. Park, B. A. Remington, S. Ross, D. Ryu, D. Ryutov, T. G. White, B. Reville, F. Miniati, A. A. Schekochihin, D. H. Froula, G. Gregori, and D. Q. Lamb, "Numerical modelling of laser-driven experiments aiming to demonstrate magnetic field

amplification via turbulent dynamo," Phys. Plasmas 24, 041404 (2017).

³⁷P. Tzeferacos, A. Rigby, A. F. A. Bott, A. R. Bell, R. Bingham, F. Cattaneo, E. Churazov, F. Fiuza, C. Forest, J. Foster, C. Graziani, J. Katz, M. Koenig, C.-K. Li, J. Meinecke, R. Petrasso, H.-S. Park, B. A. Remington, S. Ross, D. Ryu, D. Ryutov, T. G. White, B. Reville, F. Miniati, A. A. Schekochihin, D. Q. Lamb, D. H. Froula, and G. Gregori, "Laboratory evidence of dynamo amplification of magnetic fields in a turbulent plasma," Nat. Comm. 9, 591 (2018).

³⁸ A. F. A. Bott, P. Tzeferacos, L. Chen, C. A. J. Palmer, A. Rigby, A. R. Bell, R. Bingham, A. Birkel, C. Graziani, D. H. Froula, J. Katz, M. Koenig, M. W. Kunz, C.-K. Li, J. Meinecke, F. Miniati, R. Petrasso, H.-S. Park, B. A. Remington, B. Reville, J. S. Ross, D. Ryu, D. Ryutov, F. Séguin, T. G. White, A. A. Schekochihin, D. Q. Lamb, and G. Gregori, "Time resolved turbulent dynamo in a laser-plasma," Proc. Nat. Acad. Sci. USA 118, e2015729118 (2021).

³⁹S. A. Muller, D. N. Kaczala, H. M. Abu-Shawareb, E. L. Alfonso, L. C. Carlson, M. Mauldin, P. Fitzsimmons, D. Q. Lamb, P. Tzeferacos, L. Chen, G. Gregori, A. Rigby, A. F. A. Bott, T. G. White, D. Froula, and J. Katz, "Evolution of the design and fabrication of astrophysics targets for turbulent dynamo (tdyno) experiments on omega," Fusion Sci. Tech. 73, 434 (2017).

⁴⁰ A. F. A. Bott, L. Chen, G. Boutoux, T. Caillaud, A. Duval, M. Koenig, B. Khiar, I. Lantuéjoul, L. Le-Deroff, B. Reville, R. Rosch, D. Ryu, C. Spindloe, B. Vauzour, B.Villette, A. Schekochihin, D. Lamb, P. Tzeferacos, G. Gregori, and A. Casner, "Inefficient magnetic-field amplification in supersonic laser-plasma turbulence," Phys. Rev. Lett. 127, 175002 (2021).

⁴¹T. G. White, M. T. Oliver, P. Mabey, M. Kühn-Kauffeldt, A. F. A. Bott, L. Döhl, A. R. Bell, R. Bingham, R. Clarke, J. Foster, G. Giacinti, P. Graham, R. Heathcote, M. Koenig, Y. Kuramitsu, D. Q. Lamb, J. Meinecke, T. Michel, F. Miniati, M. Notley, B. Reville, D. Ryu, S. Sarkar, Y. Sakawa, M. Selwood, J. Squire, R. H. H. Scott, P. Tzeferacos, N. Woolsey, A. A. Schekochihin, and G. Gregori., "Supersonic plasma turbulence in the laboratory," Nature Commun. 10, 1758 (2019).

⁴²J. Meinecke, P. Tzeferacos, J. S. Ross, A. F. A. Bott, S. Feister, H. S. Park, A. R. Bell, R. Blandford, R. L. Berger, R. Bingham, A. Casner, L. E. Chen, J. Foster, D. H. Froula, C. Goyon, D. Kalantar, M. Koenig, B. Lahmann, C.-K. Li, Y. Lu, C. A. J. Palmer, R. D. Petrasso, H. Poole, B. Remington, B. Reville, A. Reyes, A. Rigby, D. Ryu, G. Swadling, A. Zylstra, F. Miniati, S. Sarkar, A. A. Schekochihin, D. Q. Lamb, and G. Gregori, "Strong suppression of heat conduction in a laboratory replica of galaxy-cluster turbulent plasmas," Sci. Adv. 8, eabj6799 (2022).

⁴³T. R. Boehly, D. L. Brown, R. S. Craxton, R. L. Keck, J. P. Knauer, J. H. Kelly, T. J. Kessler, S. A. Kumpan, S. J. Loucks, S. A. Letzring, F. J. Marshall, R. L. McCrory, S. F. B. Morse, W. Seka, J. M. Soures, and C. P. Verdon, "Initial performance results of the omega laser system," Optic Commun. 133, 495 (1997).

⁴⁴L. E. Chen, A. F. A. Bott, P. Tzeferacos, A. Rigby, A. Bell, R. Bingham, C. Graziani, J. Katz, M. Koenig, C. K. Li, R. Petrasso, H.-S. Park, J. S. Ross, D. Ryu, T. G. White, B. Reville, J. Matthews, J. Meinecke, F. Miniati, E. G. Zweibel, S. Sarkar, A. A. Schekochihin, D. Q. Lamb, D. H. Froula, and G. Gregori, "Transport of high-energy charged particles through spatially intermittent turbulent magnetic fields," Astrophys. J. 892, 114 (2020).

⁴⁵O. V. Gotchev, J. P. Knauer, P. Y. Chang, N. W. Jang, M. J. S. III, D. D. Meyerhofer, and R. Betti, "Seeding magnetic fields for laser-driven flux compression in high-energy-density plasmas," Rev. Sci. Instrum. 80, 043504 (2009).

⁴⁶G. Fiksel, A. Agliata, D. Barnak, G. Brent, P.-Y. Chang, L. Folnsbee, G. Gates, D. Hasset, D. Lonobile, J. Magoon, D. Mastrosimone, M. J. S. III, and R. Betti, "Note: Experimental platform for magnetized high-energy-density plasma studies at the omega laser facility," Rev. Sci. Instrum. 86, 016105 (2015).

⁴⁷J. D. Kilkenny, P. Bell, R. Hanks, G. Power, R. E. Turner, and J. Wiedwald, "High-speed gated x-ray imagers," Rev. Sci. Instrum. 59, 1793 (1988).

⁴⁸D. K. Bradley, P. M. Bell, O. L. Landen, J. D. Kilkenny, and J. Oertel, "Development and characterization of a pair of 30–40 ps x-ray framing cameras," Rev. Sci. Instrum. 66, 716 (1995).

⁴⁹E. Churazov, A. Vikhlinin, I. Zhuravleva, A. A. Schekochihin, I. Parrish, R. Sunyaev, W. Forman, H. Böhringer, and S. Randall, "X-ray surface brightness and gas density fluctuations in the coma cluster," Mon. Not. R. Astron. Soc. 421, 1123 (2012).

⁵⁰I. Zhuravleva, E. Churazov, A. A. Schekochihin, E. T. Lau, D. Nagai, M. Gaspari, S. W. Allen, K. Nelson, and I. J. Parrish, "The relation between gas density and velocity power spectra in galaxy clusters: Qualitative treatment and cosmological simulations," Astrophys. J. 788, L13 (2014).

⁵¹D. E. Evans and J. Katzenstein, "Laser light scattering in laboratory plasmas," Rep. Prog. Phys. 32, 207 (1969).

⁵²B. D. Fried and S. D. Conte, *The plasma dispersion function* (Academic Press, New York, 1961).

⁵³These estimates, which assume that the plasma's transport coefficients are accurately modelled as being that of a CH collisional plasma – a reasonable assumption, given that the mean free paths of both carbon and hydrogen ions in the plasma are much shorter than hydrodynamic length scales – are derived using the formulae given in Table 2 of the Supplementary Information of Bott *et al.*³⁸.

⁵⁴F. H. Séguin, J. A. Frenje, C. K. Li, D. G. Hicks, S. Kurebayashi, J. R. Rygg, B.-E. Schwartz, and R. D. Petrasso, "Spectrometry of charged particles from inertial-confinement-fusion plasmas," Rev. Sci. Instrum. **74**, 975 (2003).

⁵⁵C. K. Li, F. H. Séguin, J. A. Frenje, J. R. Rygg, R. D. Petrasso, R. P. J. Town, P. A. Amendt, S. P. Hatchett, O. L. Landen, A. J. Mackinnon, P. K. Patel, V. A. Smalyuk, T. C. Sangster, and J. P. Knauer, "Measuring E and B fields in laser-produced plasmas with monoenergetic proton radiography," Phys. Rev. Lett. 97, 135003 (2006).

⁵⁶M. J.-E. Manuel, A. B. Zylstra, H. G. Rinderknecht, D. T. Casey, M. J. Rosenberg, N. Sinenian, C.-K. Li, J. A. Frenje, F. H. Séguin, and R. D. Petrasso, "Source characterization and modeling development for monoenergetic-proton radiography experiments on omega," Rev. Sci. Instrum. 83, 063506 (2012).

⁵⁷C. A. J. Palmer, P. T. Campbell, Y. Ma, L. Antonelli, A. F. A. Bott, G. Gregori, J. Halliday, Y. Katzir, P. Kordell, K. Krushelnick, S. V. Lebedev, E. Montgomery, M. Notley, D. C. Carroll, C. P. Ridgers, A. A. Schekochihin, M. J. V. Streeter, A. G. R. Thomas, E. R. Tubman, N. Woolsey, and L. Willingale, "Field reconstruction from proton radiography of intense laser driven magnetic reconnection," Phys. Plasmas 26, 083109 (2019).

⁵⁸D. B. Schaeffer, W. Fox, R. K. Follett, G. Fiksel, C. K. Li, J. Matteucci, A. Bhattacharjee, and K. Germaschewski, "Direct observations of particle dynamics in magnetized collisionless shock precursors in laser-produced plasmas," Phys. Rev. Lett. 122, 245001 (2019).

⁵⁹P. T. Campbell, C. A. Walsh, B. K. Russell, J. Chittenden, A. Crilly, G. Fiksel, P. M. Nilson, A. G. R. Thomas, K. Krushelnick, and L. Willingale, "Magnetic signatures of radiation-driven double ablation fronts," Phys. Rev. Lett. 125, 145001 (2020).

⁶⁰E. R. Tubman, A. S. Joglekar, A. F. A. Bott, M. Borghesi, B. Coleman, G. Cooper, C. N. Danson, P. Durey, J. M. Foster, P. Graham, G. Gregori, E. T. Gumbrell, M. P. Hill, T. Hodge, S. Kar, R. J. Kingham, M. Read, C. P. Ridgers, J. Skidmore, C. Spindloe, A. G. R. Thomas, P. Treadwell, S. Wilson, L. Willingale, and N. C. Woolsey, "Observations of pressure anisotropy effects within semi collisional magnetized plasma bubbles," Nature Commun. 12, 334 (2021).

⁶¹ A. F. A. Bott, C. Graziani, T. G. White, P. Tzeferacos, D. Q. Lamb, G. Gregori, and A. A. Schekochihin, "Proton imaging of stochastic magnetic fields," J. Plasma Phys. 83 (2017).

⁶²M. F. Kasim, A. F. A. Bott, P. Tzeferacos, D. Q. Lamb, G. Gregori, and S. M. Vinko, "Retrieving fields from proton radiography without source profiles," Phys. Rev. E **100**, 033208 (2019).

⁶³A. Rigby, J. Katz, A. F. A. Bott, T. G. White, P. Tzeferacos, D. Q. Lamb, D. H. Froula, and G. Gregori, "Implementation of a faraday rotation diagnostic at the omega laser facility," High Power Laser Science and Engineering 6, E49 (2018).

⁶⁴N. L. Kugland, D. D. Ryutov, C. Plechaty, J. S. Ross, and H.-S. Park, "Relation between electric and magnetic field structures and their protonbeam images," Rev. Sci. Instrum. 83, 101301 (2012).

⁶⁵C. Federrath, G. Chabrier, J. Schober, R. Banerjee, R. S. Klessen, and D. R. G. Schleicher, "Mach number dependence of turbulent magnetic field amplification: Solenoidal versus compressive flows," Phys. Rev. Lett. 107, 114504 (2011).

⁶⁶R. A. Chirakkara, C. Federrath, P. Trivedi, and R. Banerjee, "Efficient highly subsonic turbulent dynamo and growth of primordial magnetic fields," Phys. Rev. Lett. **126**, 091103 (2021).

- ⁶⁷B. Srinivasan, G. Dimonte, and X.-Z. Tang, "Magnetic field generation in rayleigh-taylor unstable inertial confinement fusion plasmas," Phys. Rev. Lett. 108, 165002 (2012).
- ⁶⁸S. I. Braginskii, "Transport processes in a plasma," Rev. Plasma Phys. 1, 205 (1965).
- ⁶⁹M. G. Haines, "Magnetic-field generation in laser fusion and hot-electron transport," Can. J. Phys. **64**, 912 (1986).
- ⁷⁰C. A. Walsh, J. P. Chittenden, K. McGlinchey, N. P. L. Niasse, and B. D. Appelbe, "Self-generated magnetic fields in the stagnation phase of
- indirect-drive implosions on the national ignition facility," Phys. Rev. Lett. **118**, 155001 (2017).
- ⁷¹P. Y. Chang, G. Fiksel, M. Hohenberger, J. P. Knauer, R. Betti, F. J. Marshall, and D. D. Meyerhofer, "Fusion yield enhancement in magnetized laser-driven implosions," Phys. Rev. Lett. 107, 035006 (2011).